Article

The structure of the MICU1-MICU2 complex unveils the regulation of the mitochondrial calcium uniporter

Wenping Wu[1,†] ([iD]), Qingya Shen[1,†] ([iD]), Ruiling Zhang[1], Zhiyu Qiu[1], Youjun Wang[2] ([iD]), Jimin Zheng[1,*] ([iD]) & Zongchao Jia[3,**] ([iD])

Abstract

The MICU1-MICU2 heterodimer regulates the mitochondrial calcium uniporter (MCU) and mitochondrial calcium uptake. Herein, we present two crystal structures of the MICU1-MICU2 heterodimer, in which Ca^{2+}-free and Ca^{2+}-bound EF-hands are observed in both proteins, revealing both electrostatic and hydrophobic interfaces. Furthermore, we show that MICU1 interacts with EMRE, another regulator of MCU, through a Ca^{2+}-dependent alkaline groove. Ca^{2+} binding strengthens the MICU1-EMRE interaction, which in turn facilitates Ca^{2+} uptake. Conversely, the MICU1-MCU interaction is favored in the absence of Ca^{2+}, thus inhibiting the channel activity. This Ca^{2+}-dependent switch illuminates how calcium signals are transmitted from regulatory subunits to the calcium channel and the transition between gatekeeping and activation channel functions. Furthermore, competition with an EMRE peptide alters the uniporter threshold in resting conditions and elevates Ca^{2+} accumulation in stimulated mitochondria, confirming the gatekeeper role of the MICU1-MICU2 heterodimer. Taken together, these structural and functional data provide new insights into the regulation of mitochondrial calcium uptake.

Introduction

Mitochondrial calcium uptake is critical in cellular processes such as stimulating ATP production, modulating cell metabolism by buffering cytosolic Ca^{2+}, and preventing cellular Ca^{2+} overload, which would trigger apoptotic cell death, among other processes (Orrenius *et al*, 2003; Duchen *et al*, 2008; Balaban, 2009; Denton, 2009). Early studies revealed that Ca^{2+} enters the mitochondria through the mitochondrial Ca^{2+} uniporter, which is localized in the inner mitochondrial membrane (Kirichok *et al*, 2004; Kamer & Mootha, 2015). In vertebrates, the uniporter is a multicomponent complex that is highly selective for Ca^{2+} and consists of mitochondrial calcium uniporter (MCU) which is an ion transport pore (Baughman *et al*, 2011; De Stefani *et al*, 2011; Chaudhuri *et al*, 2013), MCU's negative regulatory subunit (MCUb) (Raffaello *et al*, 2013), metazoan-specific essential MCU regulator (EMRE) with a single transmembrane domain (Sancak *et al*, 2013), two regulatory subunits mitochondrial calcium uptake 1 and 2 (MICU1 and MICU2) with canonical EF-hand domains sensing Ca^{2+} concentrations of intermembrane space (Perocchi *et al*, 2010; Plovanich *et al*, 2013) and MICU3, a paralogue of MICU1 and MICU2, which is primarily expressed in the central nervous system (CNS) (Plovanich *et al*, 2013; Kamer & Mootha, 2015; Patron *et al*, 2018). In additional, MCU regulator 1 (MICUR1) is identified as required for MCU-dependent mitochondrial Ca^{2+} uptake (Mallilankaraman *et al*, 2012a; Tomar *et al*, 2016).

MICU1 and MICU2 are localized in the intermembrane space and form a tight heterodimer to modulate uniporter Ca^{2+} uptake by functioning as a gatekeeper (Mallilankaraman *et al*, 2012b; Csordas *et al*, 2013; Ahuja & Muallem, 2014; Kamer & Mootha, 2014). MICU1 can interact with MICU2 and MICU3 in cells with the same cysteine site through disulfide bonds, while MICU2 and MICU3 cannot form complex as demonstrated by co-IP (Patron *et al*, 2018). Additional, it has been shown that the MICU1 and MICU2 interactions also involve hydrophobic and hydrogen bonding interactions in the core domain except for disulfide bonds (Li *et al*, 2016; Kamer *et al*, 2017; Wu *et al*, 2019). The N-domain topologies of MICU2 and MICU3 are different from that of MICU1, which dictate the distinct functions of these modulators. EMRE is a metazoan-specific protein that is required for MCU-mediated

1 College of Chemistry, Beijing Normal University, Beijing, China
2 Beijing Key Laboratory of Gene Resource and Molecular Development, College of Life Sciences, Beijing Normal University, Beijing, China
3 Department of Biomedical and Molecular Sciences, Queen's University, Kingston, ON, Canada
   *Corresponding author. Tel: +86 010 58806002; E-mail: jimin_z@bnu.edu.cn
   **Corresponding author. Tel: +1 613 5336277; E-mail: jia@queensu.ca
   †These authors contributed equally to this work

Ca^{2+} uptake (Sancak *et al*, 2013; Kamer & Mootha, 2015). EMRE associates with MCU through transmembrane hydrophobic interactions, while interacts with Ca^{2+} regulator MICU1–MICU2 through electrostatic pairing contributed by poly-aspartate tail (EDDDDDD) in EMRE and polybasic sequence (KKKKR) in MICU1 (Tsai *et al*, 2016). It was reported that the MICU1 polybasic sequence also plays a role in the localization of MICU1 in the inner boundary membrane of mitochondria (Gottschalk *et al*, 2019). Several structures of MCU from fungi have been determined which demonstrate the tetrameric architectures and the Ca^{2+} selectivity mechanism (Baradaran *et al*, 2018; Fan *et al*, 2018; Nguyen *et al*, 2018; Yoo *et al*, 2018). Recently, the structure of the MCU-EMRE complex showed that EMRE triggers the dimerization of MCU and revealed the mechanism of EMRE-dependent MCU activation in metazoan (Wang *et al*, 2019). Although MCU and MCU-EMRE structures provide important knowledge about the Ca^{2+} uptake, the MICU1–MICU2 heterodimer and its regulatory mechanism are critical missing pieces.

MICU1–MICU2 functional studies indicated that the heterodimer inhibits MCU in resting conditions and relieves inhibition with increased cytosolic Ca^{2+} concentrations (Kamer & Mootha, 2014, 2015; Patron *et al*, 2014; Matesanz-Isabel *et al*, 2016). This Ca^{2+}-dependent inhibition-activation uniporter switch is dictated by the Ca^{2+}-dependent interactions between MCU and MICU1 (Petrungaro *et al*, 2015; Phillips *et al*, 2019). MCU interacts with MICU1 through the aspartic acid ring in the DIME domain of MCU; however, the identity of interaction residues in MICU1 remains controversial (Paillard *et al*, 2018; Phillips *et al*, 2019). Crystal structures of MICU1 show that MICU1 is assembled as a trimer of dimers in the apo state and changes to multiple oligomers upon Ca^{2+} binding (Wang *et al*, 2014). The MICU2 structure displays resemblances to the MICU1 structure, except for some subtle but important differences in the N-terminus domain (Kamer *et al*, 2019; Wu *et al*, 2019; Xing *et al*, 2019). In addition, Ca^{2+}-bound EF-hands in MICU1 or MICU2 increase the inter-helix angles of the EF-hands and exposes the hydrophobic regions, which occurs mainly in EF-hand 1 but not in EF-hand 2 of both proteins (Wang *et al*, 2014; Wu *et al*, 2019). Furthermore, allosteric effects resulting from EF-hands binding with Ca^{2+} (but not other divalent ions) are necessary for relieving the inhibition and triggering the MCU Ca^{2+} uptake (Kamer *et al*, 2017, 2018).

Although many MICU1–MICU2 complex studies have been documented, several fundamental questions remain to be answered. How do Ca^{2+} ions affect heterodimer conformational changes? How does EMRE interact with MICU1 in both Ca^{2+}-free and Ca^{2+}-bound conditions? How does the heterodimer activate the uniporter in high cytoplasmic Ca^{2+} concentrations and inhibit MCU under resting conditions? Herein, we present two pairs of different MICU1–MICU2 heterodimers crystal structures at 2.1 Å resolution, in which both Ca^{2+}-free and Ca^{2+}-bound EF-hands are observed. Interface I defines electrostatic interactions crucial for the Ca^{2+}-free form, whereas interface II features hydrophobic interactions that are significant for the Ca^{2+}-bound form. Furthermore, we have identified a Ca^{2+}-enhanced alkaline groove in MICU1 that is responsible for interacting with EMRE. The discovery of such a Ca^{2+}-dependent interactions switch between MICU1-MCU and MICU1-EMRE is significant for understanding the conversion mechanism between different functions.

Results

Structure determination of Ca^{2+}-free and Ca^{2+}-bound MICU1–MICU2 heterodimers

We purified two MICU1–MICU2 complexes (His_6-tagged MICU1 and tagged-free MICU2, His_6-tagged MICU2, and tagged-free MICU1) under both EGTA and $CaCl_2$ conditions. The size-exclusion chromatography (SEC) results indicate that the MICU1–MICU2 complex displays a monodisperse peak with a molecular weight of ~ 80 kDa under both 2 mM EGTA and $CaCl_2$ conditions (Fig EV1A, B, E, and F). Additionally, the MICU1–MICU2 heterodimer had a high purity with a stoichiometric ratio of ~ 1:1, as illustrated by SDS–PAGE (Fig EV1C, D, G, and H). Unfortunately, despite extensive efforts, the four aforementioned high-purity samples did not yield crystal hits. To circumvent the difficulty of heterodimer crystallization, we introduced a flexible linker (GSGSGSGSGSGSGSGS) between the C-terminus of MICU1 and the N-terminus of MICU2. The MICU1–MICU2 chimaera displayed identical SEC retention volumes to the MICU1–MICU2 complex in both EGTA and $CaCl_2$ conditions (Fig 1A and B). The chimaera construct yielded crystal hits in the EGTA condition, which were optimized to produce diffraction-quality crystals. Finally, the chimaera structure was determined by molecular replacement and refined at a resolution of 2.1 Å with $R_{work} = 19.39\%$ and $R_{free} = 22.67\%$. The asymmetric unit contains two molecules of the MICU1–MICU2 chimaera, which pack in an antiparallel mode with a face-to-face configuration, forming a barrel-like architecture with a large cavity in the middle (Fig 1C). Importantly, in one of the MICU1–MICU2 molecules, there are unambiguous electron densities in two EF-hands (one in MICU1 EF-hand 2 and the other in MICU2 EF-hand 1; Fig EV2A and B). The two metal ions adopt a pentagonal bipyramid geometry with seven ligands and show a bidentate interaction with the Glu_{12} (position 12 of the loop) carboxyl, which is typical for Ca^{2+}-bound EF-hand proteins (Fig EV2C and D). This MICU1–MICU2 chimaera molecule represents a partial Ca^{2+}-bound MICU1–MICU2 heterodimer.

MICU1–MICU2 heterodimers interfaces

The partial Ca^{2+}-bound and Ca^{2+}-free MICU1–MICU2 chimaeras feature an antiparallel packing mode in which EF-hands 1 are localized in the heterodimer interface regions. The interactions of Ca^{2+}-free and Ca^{2+}-bound heterodimers are defined by two interfaces (Fig 2B). In the Ca^{2+}-free heterodimer, the interaction interface I involves extensive electrostatic interactions contributed by the α-helixes of MICU1 EF-hand 1 (referred to as $M1\_EH_11$ and $M1\_EH_12$) and the α-helixes of MICU2 EF-hand 2 pair (referred to as $M2\_EH_{2p}1$, $M2\_EH_{2p}2$, $M2\_EH_{2p}3$, and $M2\_EH_{2p}4$; detailed interaction analyses can be found in the Expanded View; Fig 2A left and middle). It is noted that Arg352 makes the greatest contribution to the interaction interface by forming hydrogen bonds with several key interfacial residues (Fig 2A left), substantiating the pull-down experiment results from our previous report (Wu *et al*, 2019). Intriguingly, there is a lack of electrostatic interactions in interface II involving the MICU1 EF-hand 2 pair α-helixes (referred to as $M1\_EH_{2p}1$, $M1\_EH_{2p}2$, $M1\_EH_{2p}3$, and $M1\_EH_{2p}4$) and the MICU2 EF-hand 1 α-helixes (referred to as $M2\_EH_11$ and $M2\_EH_12$), while
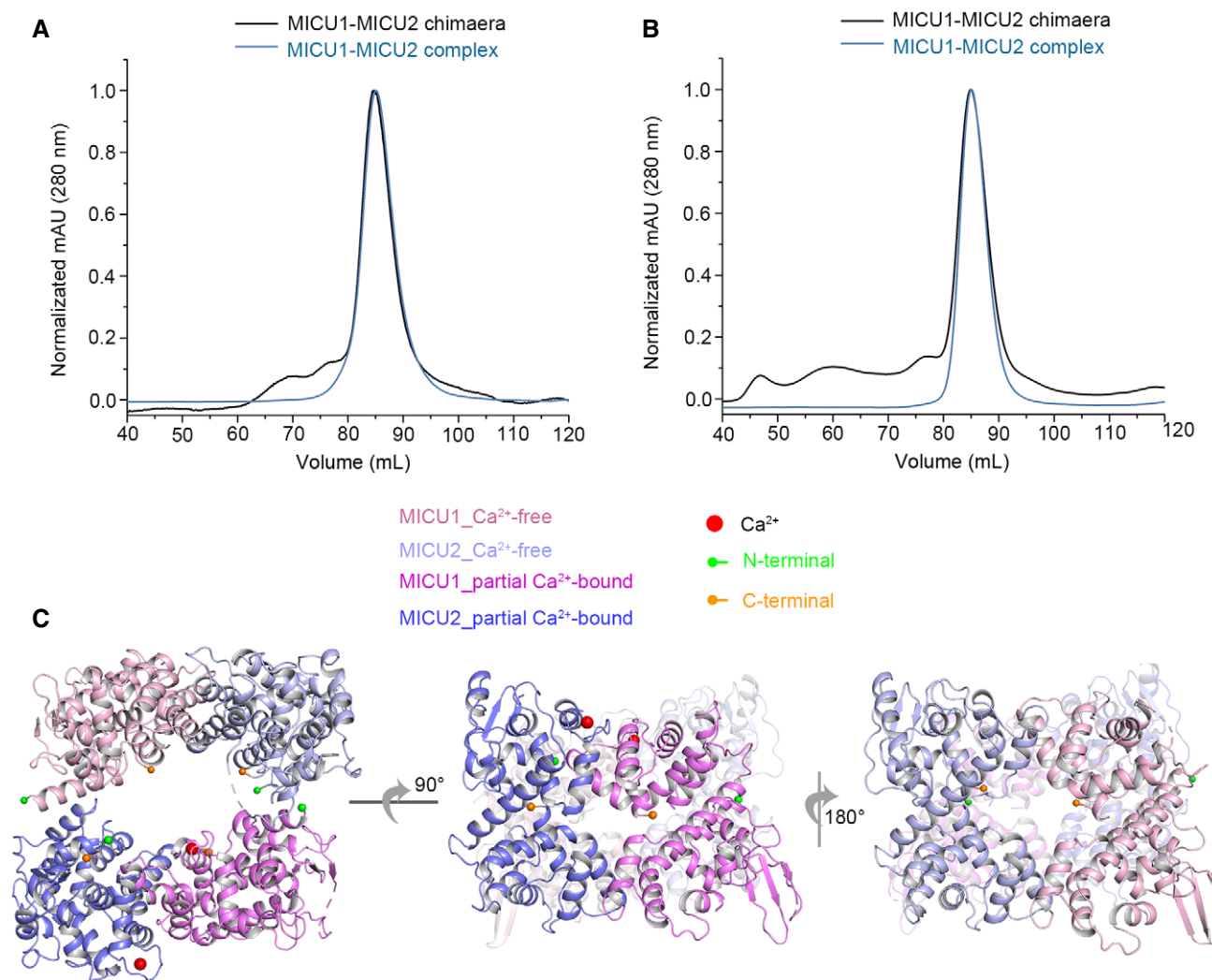
Figure 1. Biochemical and structural characterizations of the MICU1-MICU2 chimaera.

A, B   Representative size-exclusion chromatography profiles of the MICU1–MICU2 complex and chimaera in 2 mM EGTA (A) and 2 mM $CaCl_2$ (B) conditions.

C   Top (left) and side (middle and right) views of the overall MICU1–MICU2 chimaera structure with four molecules in a crossed arrangement. Ca^{2+}-free and partial Ca^{2+}-bound MICU1 structures are colored in pink and magenta, respectively. The Ca^{2+}-free and partial Ca^{2+}-bound MICU2 structures are colored in light blue and blue, respectively. The red, green, and orange spheres represent Ca^{2+}, N-, and C-terminus.

weak hydrophobic interactions exist (Fig 2A right; detailed interaction analyses can be found in the Expanded View).

The partial Ca^{2+}-bound heterodimer interface I is similar to that in the Ca^{2+}-free heterodimer (Fig 2B right). In interface II, the hydrophobic interactions between hydrophobic residues Phe383, Met386 in MICU1, and the hydrophobic pocket in MICU2 EF-hand 1 constitute the primary interaction mode (Fig 2C right), which correspond to our previous pull-down experiments (Wu *et al*, 2019). In addition to the hydrophobic interaction, several hydrogen bonding or electrostatic interactions are also observed (Fig 2C left; detailed analyses can be found in the Expanded View). In many EF-hand-containing proteins, Ca^{2+} binding to the EF-hand shortens the distance between Asp_1 (position 1 of the loop) and Glu_{12} and expands the interhelical bottom angle, thus creating a hydrophobic pocket for recruiting hydrophobic residues or domains (Gifford *et al*, 2007). As shown by structural analyses, Phe383 inserts into

the hydrophobic pocket that is created by Ca^{2+} binding to EF-hand 1 of MICU2, just like embedding a wedge (Fig 2D). Based on the structural analyses, the interaction pattern of the partially Ca^{2+}-bound heterodimer appears to represent the "transition" conformation between the Ca^{2+}-free and Ca^{2+}-bound states.

Several key residues were previously screened by a scanning mutagenesis method using glutathione *S*-transferase (GST) pull-down experiments in both absence and presence of 2 mM $CaCl_2$ (Wu *et al*, 2019). The GST pull-down experiments confirmed that the Glu242 in MICU1 and Arg352 in MICU2 are the crucial residues participating the interaction in the absence of Ca^{2+}, whereas Phe383 in MICU1 and Glu196 in MICU2 contribute to the hetero-dimer formation in the Ca^{2+}-bound state (Wu *et al*, 2019). To further probe MICU1–MICU2 interactions, we created more mutants based on our structures (Fig EV3 and Appendix Fig S1). These mutants include MICU1_Q253A, MICU1_Q398A, MICU1_E427A,
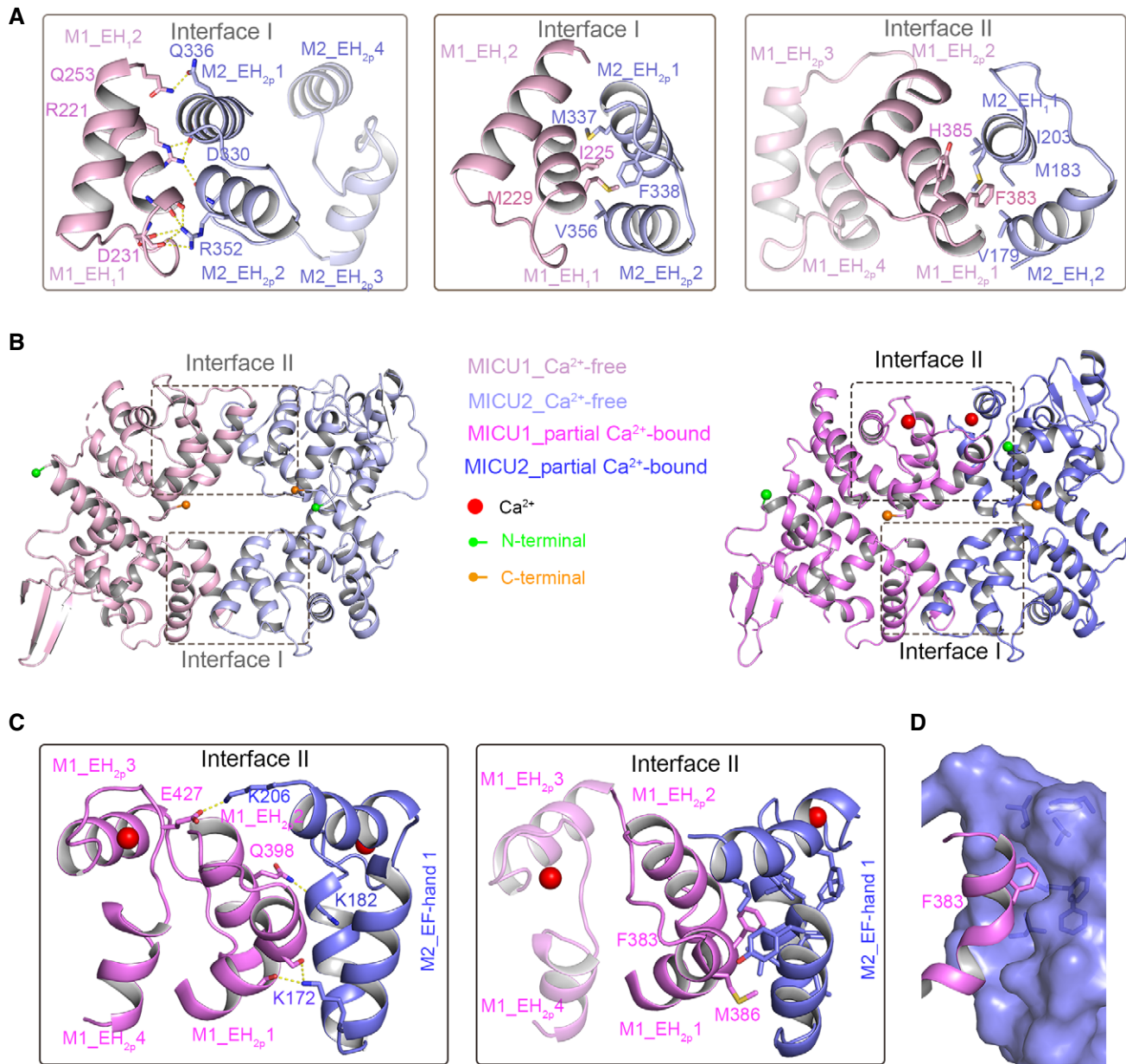
Figure 2.   Interfaces of MICU1-MICU2 Ca²⁺-free and partial Ca²⁺-bound states.

A   Close-up view of Ca²⁺-free MICU1–MICU2 interfaces I (left and middle) and II (right). The atomic interactions at the interface I consist of mainly electrostatic (left) and weak hydrophobic (middle) interactions, while interface II mainly contains hydrophobic interactions (right).

B   MICU1 interacts with MICU2 at two major interfaces.

C   Close-up views of the partial Ca²⁺-bound MICU1–MICU2 interface II. The atomic interactions at interface II consist of weak electrostatic (left) and strong hydrophobic (middle) interactions. The red, green, and orange spheres represent Ca²⁺, N-, and C-terminus.

D   The surface-rendered MICU2 hydrophobic pocket shows the interaction at interface II.

MICU2_K206A, and MICU2_Q336A. We first investigated whether the MICU1 mutants would affect the heterodimer interactions under the two Ca²⁺ conditions. Our results show that MICU2 can interact with MICU1_Q253A, MICU1_Q398A, and MICU1_E427A in both presence and absence of Ca²⁺ whether the MICU1 mutants or MICU2_WT construct were used as baits (Fig EV3A–C, Appendix Fig S1C–E). But MICU1_Q253A and MICU1_E427A mutants reduced the interactions in the Ca²⁺-free condition

compared with that in the presence of Ca²⁺ when GST-MICU1 mutants were used as baits (Appendix Fig S1C and E). Next, we analyzed the effects of MICU2 mutants in Ca²⁺-free and Ca²⁺-bound heterodimers. GST-MICU2_K206A pulled down MICU1_WT in both absence and presence of Ca²⁺, whereas MICU2_Q336A mutant displayed weakened interaction with MICU1 in these conditions (Fig EV3D and E). The reverse pull-down experiments also yielded the same conclusions when MICU1_WT was used as the bait

(Appendix Fig S1A and B). The results indicate that these residues might participate in the MICU1–MICU2 interaction in the absence of Ca^{2+}, but are not the key sites.

Conformational changes in the Ca^{2+}-free and Ca^{2+}-bound heterodimers

We aligned the backbone atoms between the two states structures for better expounding the discrepancy of two structures. The overall structures of the two heterodimers (with and without Ca^{2+} bound) were similar with RMSD value of 2.045 Å. Evident from the overall structure alignment, the EF-hand 1 of MICU2 and EF-hand pair 2 of MICU1 display significant conformational changes (Fig 3A). It is evident that Ca^{2+} binding serves as a conformational switch to govern the EF-hand close-to-open conformational transition by altering the interhelical angle (Gifford *et al*, 2007). Upon Ca^{2+} binding, the EF-hand 1 α-helixes in MICU2 rotate from an antiparallel arrangement in the apo state to an approximately perpendicular mode with an interhelical angle of 90° (Fig 3A middle, Appendix Fig S2B and Movie EV1). The EF-hand pair 2 of MICU1 in the Ca^{2+}-bound state rotates toward MICU2 compared to the Ca^{2+}-free state (Fig 3A right and Movie EV1). On the other hand, the MICU1 EF-hand 2, which coordinates Ca^{2+}, maintains the same interhelical angle compared to that without the occupied Ca^{2+} (Appendix Fig S2A).

Next, we calculated the buried surfaces in the two structures. The binding surface of the partial Ca^{2+}-bound heterodimer ($\sim$ 1,426 Å^2) is larger than that of the Ca^{2+}-free heterodimer ($\sim$ 1,119 Å^2), which is consistent with our structural analysis. The calculation of the buried surface area provides direct evidence to demonstrate that Ca^{2+} binding to EF-hands enhances the compactness and, by extension, stability of the complex. Additionally, the Ca^{2+}-bound lobes extend $\sim$ 58 Å in width, which is narrower than that in the Ca^{2+}-free lobes, which is $\sim$ 64 Å (Appendix Fig S3); this result substantiates the notion that Ca^{2+} binding significantly tightens the heterodimer.

Our partial Ca^{2+}-bound structure features both Ca^{2+}-free and Ca^{2+}-bound characteristics that have helped shed light on the transition from the apo state to the Ca^{2+}-bound state. Next, we constructed a fully Ca^{2+}-bound model. The extensive structural information from numerous Ca^{2+}-bound EF-hands in the literatures help us to readily build this model using the partial Ca^{2+}-bound heterodimer as a starting template. The comparison of the three heterodimers (apo, partial and fully Ca^{2+}-bound) shows that the conformational changes primarily occur in the EF-hand domains, particularly in EF-hands 1 in both MICU1 and MICU2, which expose the hydrophobic pockets upon Ca^{2+} binding (Fig 3B and Movies EV1 and EV2). Furthermore, the EF-hand pair 2 in MICU1 and the EF-hand 1 in MICU2 rotate considerably in the partially or fully Ca^{2+}-bound heterodimers that may have implications in regulating the Ca^{2+} uptake in the uniporter (Fig 3A and B).

The alkaline groove of MICU1 mediates the interaction with EMRE

The polybasic sequence (KKKKR) of MICU1 mediates the interaction with EMRE (Tsai *et al*, 2016); however, this sequence in our structure is unresolved, likely due to its flexibility. To make the N-

terminus of the MICU1 construct more rigid, we introduced a fusion protein (T4 lysosome) in the MICU1 N-terminus and determined the new T4L-MICU1–MICU2 complex structure in the Ca^{2+}-free state at a resolution of 3.3 Å. The overall structure is similar to our previous complex devoid of the T4L fusion protein in which the two molecules of the heterodimers are assembled in a face-to-face configuration with a twofold symmetry (Appendix Fig S4A and B). Fortunately, the polybasic sequence (KKKKR) is now observed in MICU1, which is a short α-helix (Appendix Fig S4C).

EMRE likely functions to anchor the MICU1–MICU2 heterodimer to prevent the dissociation from the channel with increasing Ca^{2+} concentrations in the cytosol (Petrungaro *et al*, 2015; Tsai *et al*, 2016). To better understand the spatial relationship among various components in the uniplex, we performed charge potential analyses of both the Ca^{2+}-free and partial Ca^{2+}-bound heterodimers. MICU1 α-helixes (referred to as M1_CH1 and M1_CH2) are located at the protein edge and display an increased positive charge in the presence of Ca^{2+} (Figs 3D and EV4). This charge distribution is reflected by a large positively charged groove consisting of M1_CH1, M1_CH2, and the polybasic α-helix (Appendix Fig S4C and D). The electron positivity of Ca^{2+} attracts the acidic residues in the EF-hand loop toward the central loop area, whereas these acidic residues are repelled in the apo state. Because of the Ca^{2+} repulsion and lacking of attraction of negatively charged residues, the side chains of the KRKK motif (Lys340, Arg347, Lys350, and Lys351) in M1_CH1 helix and Arg325 in M1_CH2 are repelled toward the groove upon Ca^{2+} binding (Fig 3C). Considering that EMRE has the negatively charged poly-aspartate tail, this alkaline groove becomes the most reasonable place for MICU1 and EMRE to interact. These conformational changes may provide a favorable condition for the interaction between MICU1 and EMRE. Upon Ca^{2+} binding, the KRKK motif in MICU1 further strengthens the interaction between EMRE and MICU1 by enhancing the positively charged areas to compensate for the loss of the interaction with the channel.

To confirm this speculation, we synthesized an EDDDDDD peptide to examine its interaction with MICU1 using microscale thermophoresis (MST) for understanding the process of Ca^{2+} signal from modulators to channel. We designed three mutants, including MICU1_poly$_K$E that replaced the polybasic motif with EEEEE sequence, MICU1_$_{KRKK}$EEEE that replaced four curial residues (Lys340, Arg347, Lys350, and Lys351) with Glu, and MICU1_R325E. Our results show that the EMRE peptide could indeed interact with MICU1 in both conditions, although this interaction is weaker in the presence of EGTA (Fig 4C). Furthermore, the three MICU1 mutants all lost the interactions with the peptide in the presence of EGTA (Fig 4A). MICU1_$_{KRKK}$EEEE perturbs the interaction with the EMRE peptide in the presence of Ca^{2+}, while MICU1_poly$_K$E and MICU1_R325E retain the interactions with the EMRE peptide, similar to the wild-type protein (Fig 4B). The MST results are in accordance with the structural analysis showing that the alkaline groove mediates the EMRE and MICU1 interaction and also enhances this electrostatic interaction in the presence of Ca^{2+}. As revealed in the structure, KRKK motif and Arg352 rotate toward the groove interior to strengthen the EMRE-MICU1 interaction and, as a result, these mutants in Ca^{2+}-binding state had little effect compared with the Ca^{2+}-free condition. Furthermore, the isothermal titration calorimetry (ITC) curve demonstrates that the EMRE peptide interacts with MICU1 at an approximate stoichiometric ratio of 1:1 (Fig 4D), in
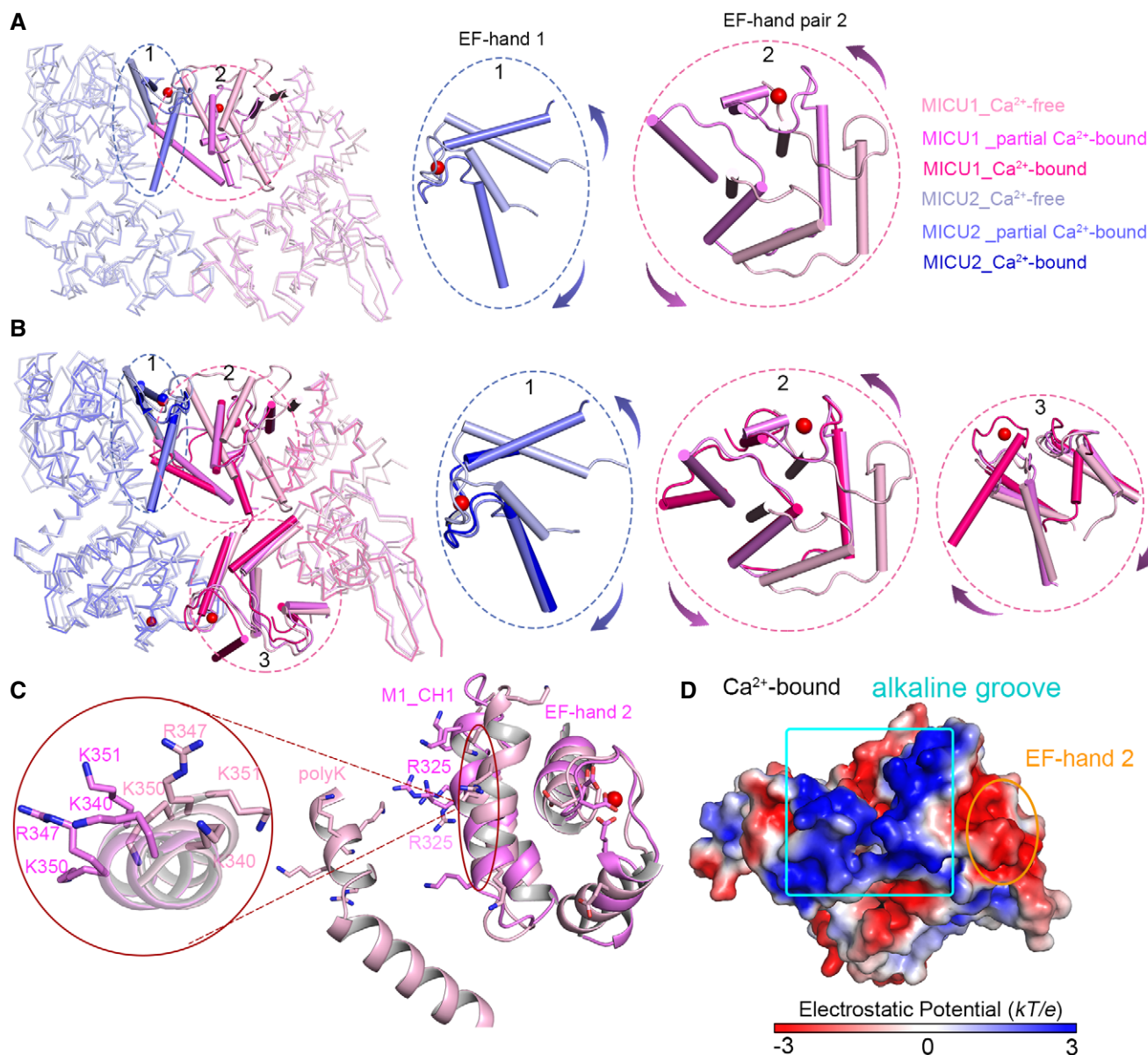
Figure 3. Structural alignments of MICU1–MICU2 with different numbers of Ca²⁺ ions bound.

A Structural alignment of Ca²⁺-free and partial Ca²⁺-bound MICU1–MICU2 heterodimers, as well as critical substructures with conformational changes indicated by numbered dashed circles. Middle and right, close-up view of the MICU2 EF-hand 1 (middle, circle 1) and MICU1 EF-hand pair 2 (right, circle 2) conformational changes upon Ca²⁺-binding. The important α-helixes are highlighted as cylinders. The red sphere represents Ca²⁺.

B Structural alignment of Ca²⁺-free, partial Ca²⁺-bound, and fully Ca²⁺-bound MICU1–MICU2 model heterodimers and important substructures with conformational changes are indicated by numbered dashed circles. Three different MICU1 and MICU2 molecules are individually shown in similar colors, and the colors changing from light to dark correspond to an increase in Ca²⁺ numbers. Circles 1, 2, and 3: close-up views of MICU2 EF-hand 1, MICU1 EF-hand pair 2, and MICU1 EF-hand 1 conformational changes upon Ca²⁺-binding, respectively. Important α-helixes are highlighted as cylinders. The red sphere represents Ca²⁺.

C Conformational changes of the alkaline groove between T4L fusion Ca²⁺-free MICU1–MICU2 and partial Ca²⁺-bound MICU1–MICU2 heterodimers. Inset, KRKK residues in the alkaline groove rotate upon Ca²⁺ binding.

D Electrostatic surface potential of the alkaline groove in partial Ca²⁺-bound structure. The gradient shown is from −3 (acidic, red) to +3 (basic, blue) kT/e.

line with the ~ 100 kDa migration of MICU1–MICU-EMRE complex in the uniporter assembly experiments *in vivo* (Opalinska & Janska, 2018).

Encouraged by the observation of the interaction *in vitro*, we next asked the question of whether this peptide would compete with the endogenous EMRE in cells. We synthesized a mitochondria-targeting EMRE peptide (mt-EMRE peptide) that contains a supplemental mitochondria-targeting sequence at the N-terminus of the peptide as previously reported (Cerrato *et al*, 2015). To detect the location of EMRE peptide, we used the mt-EMRE peptide conjugated with fluorescence probe 5(6)-carboxytetramethylrhodamine (TAMRA). Cells were transiently transfected mEmerald-Mito-7 that

specifically targets the mitochondrial as a mitochondrial marker (Planchon *et al*, 2011) and treated with TAMRA-mt-EMRE peptide for fluorescence microscopy analysis. The merged image and quantitative co-localization analysis illuminate the co-localization between our peptide and mEmerald-Mito-7, demonstrating that mt-

EMRE peptide can be imported into mitochondria to exert its function (Appendix Fig S5). We further used the genetically encoded ratiometric Ca^{2+} indicator mt-riG6 m to monitor the Ca^{2+} mitochondrial matrix signals (Li *et al*, 2020). Clearly, the fluorescence ratio of mt-riG6 m in cells treated with the mt-EMRE peptide was
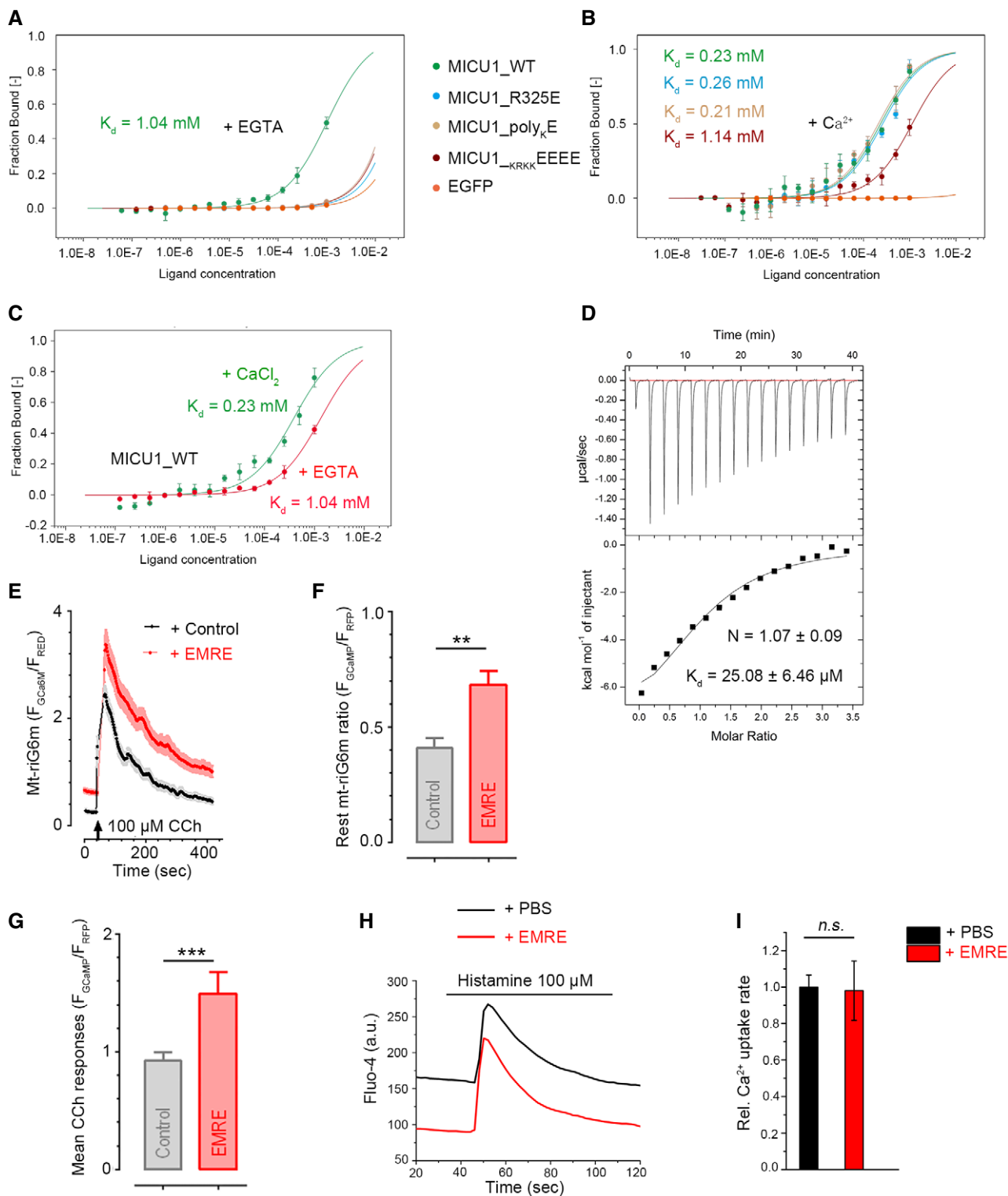

Figure 4.

◀

Figure 4. The characterization of interactions between EMRE peptide and MICU1 *in vitro* and EMRE peptide competition in cells.

A   The binding of fluorescently (GFP) labeled MICU1 and mutants to EMRE peptide shown by MST in the presence of EGTA.
B   The binding of fluorescently (GFP) labeled MICU1 and mutants to EMRE peptide were analyzed with MST in the presence of Ca^{2+}.
C   Comparison of binding of MICU1 and EMRE peptide in both conditions.
D   MICU1–MICU2 heterodimer interacts with the EMRE peptide at a 1:1 ratio.
E   Carbachol (CCh)-induced representative traces of mitochondrial calcium uptake in HEK cells treated with mt-EMRE and scramble peptides. Solid lines, mean; shaded regions, ± SEM, $n = 3$.
F   Resting mitochondrial Ca^{2+} levels in mt-EMRE and scramble peptides treated cells, evaluated via ratiometric imaging of the mitochondrial targeted mt-riG6m. Mean ± SD, Student's *t*-test, **$P < 0.01$, $n = 3$.
G   Mean mitochondrial Ca^{2+} peaks response to 100 μM CCh. Mean ± SD, Student's *t*-test, ***$P \leq 0.001$, $n = 3$.
H   Representative $[Ca^{2+}]_c$ clearance traces of U2OS cells treated with PBS and mt-EMRE peptide.
I   Quantification of mitochondria Ca^{2+} uptake rate in response to 100 μM histamine. Mean ± SD, Student's *t*-test, n.s., not significant, $n = 4$.

Data information: Error bars for some points are too small to be visible.

stronger than that in cells treated with the scramble peptide in resting conditions (Fig 4E and F). This result demonstrates that the mt-EMRE peptide effectively competed with endogenous EMRE which probably weakened the interaction between the MICU1–MICU2 complex and the channel, resulting in the reduction of threshold in resting conditions. Moreover, in mt-EMRE treated cells, the $[Ca^{2+}]_m$ peak evoked by carbachol was markedly greater, indicating elevated Ca^{2+} accumulation in mitochondria due to reduction of threshold (Fig 4E and G). With this in mind, we measured extra-mitochondrial Ca^{2+} clearance using cytoplasmic Ca^{2+}-sensitive fluorescent dye. $[Ca^{2+}]_c$ measurements showed a marked enhancement of the transient rise evoked by stimulation with 100 μM histamine in the presence of mt-EMRE peptide, similar to the control cells (Figs 4H and EV5A). The kinetics of Ca^{2+} clearance in both conditions showed negligible differences (Figs 4I and EV5B). In conclusion, these results demonstrate that mt-EMRE peptide reduced uniporter threshold, resulting in consequently Ca^{2+} accumulation in mitochondria under resting and stimulation conditions. Interestingly, the peptide did not affect the kinetics of mitochondrial Ca^{2+} uptake in response to histamine.

Discussion

We have determined structures of two crystallographically independent MICU1–MICU2 heterodimers with barrel-like configuration (Fig 1C), providing new insights into mitochondrial Ca^{2+} uptake modulation. In addition to the "barrel-like" arrangement, the "linear" packing mode of the two complexes is observed (Appendix Fig S6). The adjacent MICU2 molecules in the middle are assembled in a back-to-back mode (Appendix Fig S6). In fact, the crystal packing shows that the MICU1 monomer is not within an interaction distance to associate with another MICU1 monomer, in neither a back-to-back nor a face-to-face configuration. Our structure appears to represent a "transition state" between apo and holo structures, which is informative since the hybrid structure simultaneously displays both Ca^{2+}-free and Ca^{2+}-bound characteristics (Fig 1C). Interfaces I and II seem to play different roles in prompting interaction modes; they are critical for the Ca^{2+}-free and Ca^{2+}-bound MICU1–MICU2 association through electrostatic and hydrophobic interactions, respectively (Fig 2). Recently, a human Ca^{2+}-free MICU1–MICU2 complex structure was reported, which displays the face-to-face configuration with salt bridge interaction sites between MICU1 and MICU2 (Park *et al*, 2020), in agreement

with our chimaera structure. The superimposition between the Ca^{2+}-free complex and our Ca^{2+}-free chimaera structure shows negligible discrepancy, yielding RMSD value of only 1.28 Å (Appendix Fig S7). Thus, the previous pull-down results and the recently reported Ca^{2+}-free MICU1–MICU2 complex structure substantiate the notion that our chimaera heterodimer does not appear to introduce any biases (Wu *et al*, 2019; Park *et al*, 2020).

We introduced T4L to afford some stability of polybasic KKKKR sequence in MICU1, and we observed at least one of its main conformations. Although T4L may affect the "native" position of the N-terminus since its presence would reduce the dynamic range of conformational flexibility, it should not fundamentally affect the main orientation of KKKKR helix which protrudes out from the main structure and into the open space (Appendix Fig S4A–C). If KKKKR fragment were closely associated with the MICU1–MICU2 complex (i.e., not in the open space), its electron density would not be so poor and some (if not all) of its structure would have been observed. This standalone helix and other basic residues (KRKK motif and Arg325) constitute the alkaline groove that mediates the interaction of MICU1-EMRE. The alkalinity of the groove is increased in the presence of Ca^{2+} which facilitates MICU1-EMRE interaction, and the disruption of this interaction will lead to $[Ca^{2+}]_m$ disorder. We proceeded with assessing the uniporter threshold of Ca^{2+} uptake using mt-EMRE peptide in competition assays. The mt-EMRE peptide can effectively compete with the endogenous EMRE and destabilize the intrinsic EMRE-MICU1 association, resulting in the reduction of threshold in resting conditions (Fig 4E and F), whereas the kinetic of mitochondria Ca^{2+} uptake was not affected (Figs 4I and EV5B).

Very recently, a cryo-EM structure of the uniporter core complex (MCU-EMRE-MICU1–MICU2) was reported, revealing a rather unexpected stoichiometry of 4:4:1:1 (Fan *et al*, 2020). The super-complex structures show that MICU1 directly blocks the Ca^{2+} pore in resting conditions through its arginine/lysine region interacting with aspartic acid ring in MCU channel entrance, while MICU1 dissociates from MCU and, together with MICU2, drifts to the side of channel in the active condition (Fan *et al*, 2020). Although the interaction region of EMRE-MICU1 was unresolved in the super-complex structure, the general direction of the interaction region points to our proposed alkaline groove pocket, providing support to our result. The interaction of MICU1-MCU was significantly weakened in the presence of Ca^{2+} (Tsai *et al*, 2016; Phillips *et al*, 2019; Fan *et al*, 2020), while MICU1-EMRE interaction was promoted in this condition. Thus, we put forward an interactions switch model that propels Ca^{2+} signal
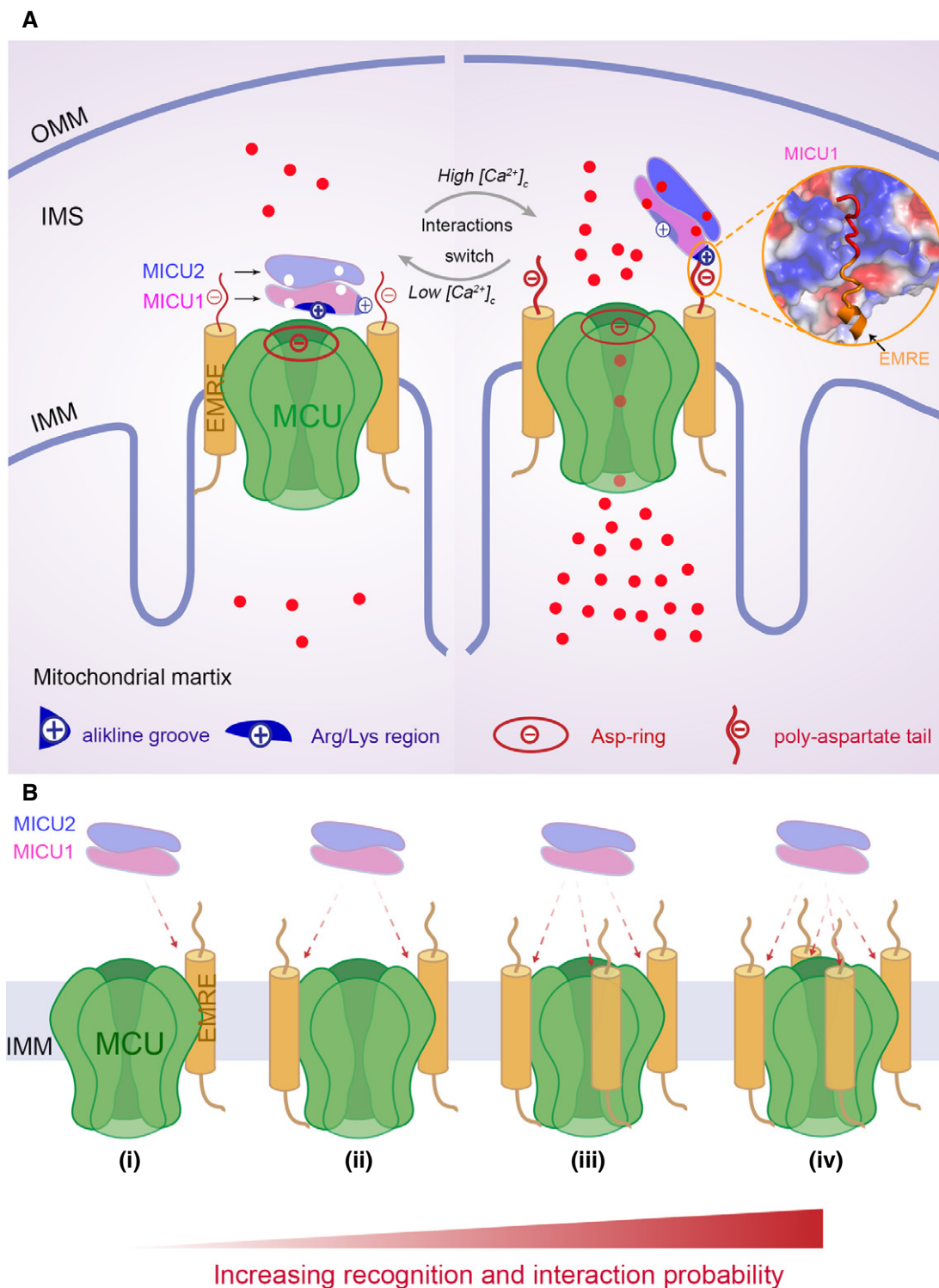
Figure 5. Model of the uniporter regulatory mechanism.

A Model of MCU Ca^{2+} uptake modulatory mechanism by interaction switch. In resting conditions, MICU1–MICU2 heterodimer associates with MCU pore to prevent Ca^{2+} transporting. In the stimulated condition, MICU1–MICU2 heterodimer enhances the interaction with EMRE by increasing the positive charge of alkaline groove and disassociates form MCU, resulting in opening the gate and activating the Ca^{2+} channel. Inset shows modeled interaction between the EMRE C-terminal poly-aspartate tail and MICU1 alkaline groove.

B Probability model for MICU1–MICU2 heterodimer to recognize and interact with the channel. As the number of EMRE molecules increases, the interaction sites between MICU1–MICU2 heterodimer and channel increase. Consequently, the probability for MICU1 to recognize and interact with the channel is increased, enhancing the regulatory function of MICU1–MICU2.

transmission from the regulator to the channel (Fig 5A). While weakly interacting with EMRE, MICU1 mainly associates with MCU in resting conditions to gate the Ca^{2+} channel and switches to dominantly binding to EMRE with the increasingly positive charge of alkaline groove at high Ca^{2+} levels, releasing Ca^{2+} into the mitochondria matrix (Fig 5A). In this switch scenario, the MICU1–MICU2 heterodimer primarily undergoes two allosteric conformational changes that (i) induces the hydrophobic pocket of MICU2 to attract Phe383 of MICU1 upon Ca^{2+} binding which may result in MICU1 dissociating from MCU and (ii) promotes the positive charge of the alkaline groove which transmits the Ca^{2+} signal to EMRE by tightening the MICU1-EMRE interaction. The Ca^{2+}-dependent interactions switch model readily complements the transition mechanism between gatekeeping and cooperative functions, reflecting the conferred regulatory and scaffold functions of EMRE. Although the two super-complexes structural characterizations can intuitively explain the gatekeeping and activation mechanisms to some extent (Fan *et al*, 2020), they have raised an important question—why there are varying and multiple copies of EMRE molecule in uniplex?

Recently, Payne *et al* (2020) reported that there exists variable number of EMRE per channel (1–4) *in vivo* and increasing number of EMRE enhances the gatekeeping function. According to the super-complex structures (Fan *et al*, 2020), the tetrameric MCU channel possesses fourfold symmetry which is flat in the pore entrance and accommodates only one MICU1–MICU2 heterodimer. In the case of 4 molecules of EMRE, the heterodimer can locate in the any of the four positions by rotating 90° around the channel center, yielding equivalent interaction environment. When there are less copies of EMRE, the fourfold symmetry is perturbed and the heterodimer would be "guided" to interact with where EMRE(s) resides, as a result of the electrostatic interaction between the MICU1's alkaline groove and EMRE's poly-aspartate tail which is weaker in resting conditions and stronger in activated state. Thus, the number of EMRE molecules corresponds to the number of probable locations of MICU1–MICU2 heterodimer. As the number of EMRE increases, the probability of recognition and interaction for MICU1–MICU2 heterodimer to associate with the channel also increases, which can improve the gatekeeping efficiency (Fig 5B) and is in agreement with the literature (Payne *et al*, 2020). Regardless the stoichiometric ratio of channel and EMRE, EMRE always tethers MICU1–MICU2 to MCU, maintaining the interaction switch to accomplish the opposite function transition.

In conclusion, we have determined the MICU1–MICU2 heterodimer complex structures in two Ca^{2+} states and revealed conformational changes from the Ca^{2+}-free condition to the Ca^{2+}-bound condition. The Ca^{2+}-dependent interactions switch has solidified the transition mechanism between opposite functions—gatekeeping and activation. Our results establish a framework for understanding the regulatory mechanism of MICU1–MICU2 and provided insights into EMRE's guiding and tethering function.

Materials and Methods

Protein cloning, expression, and purification

MICU1 (BC004190.2, residues 97–444) and MICU2 (BC031089.1, residues 85–406) were connected by a flexible linker

(GSGSGSGSGSGSGSGSGS). The MICU1–MICU2 chimaera gene was cloned into the pET-28b(+) plasmid with an N-terminus His_6-tag and transformed into the BL21(DE3) *Escherichia coli* strain. For the T4L-MICU1–MICU2 chimaera, the same flexible linker was used between MICU1 and MICU2. The T4 lysozyme gene was cloned into the pET-28b(+) plasmid between NcoI and NdeI restriction enzyme sites with an N-terminus His_6-tag. MICU1–MICU2 positioned after T4L was cloned between the NdeI and XhoI sites. The recombination proteins were expressed in 1 l Luria Broth (LB) medium at 37°C until the $OD_{600\ nm}$ reached ~ 0.8, and then, the cultures were induced with isopropyl β-D-1-thiogalactopyranoside (IPTG) at the final concentration of 0.5 mM. Cells were cultivated at 16°C for 20 h before harvesting. The harvested pellet was resuspended in buffer I (20 mM HEPES pH 8.0, 300 mM NaCl, 0.3% Triton X-100, and 1 mM phenyl methane sulfonyl fluoride with or without 2 mM $CaCl_2$) and sonicated for lysis. After centrifugation for 30 min at 18,000 *g*, the supernatant was loaded onto a Ni-NTA gravity column pre-equilibrated with buffer I. The protein was washed with buffer II (20 mM HEPES pH 8.0, 300 mM NaCl, and 30 mM imidazole with or without 2 mM $CaCl_2$) for 100 ml. Finally, the protein was eluted in buffer III (20 mM HEPES pH 8.0, 300 mM NaCl, and 500 mM imidazole with or without 2 mM $CaCl_2$). The eluted protein was concentrated until the total volume reached 1 ml and was then purified using SEC. Before running the ÄKTA purifier, the SEC column was equilibrated with buffer IV (20 mM HEPES pH 8.0, 300 mM NaCl, and 2 mM DTT with either 2 mM EGTA or 2 mM $CaCl_2$). The protein was detected at an absorption wavelength of 280 nm, and the sample was collected at the corresponding retention volume.

Crystallization and X-ray data collection

The two proteins (MICU1–MICU2 and T4L-MICU1–MICU2) were purified in buffer containing 20 mM HEPES pH 8.0, 300 mM NaCl, 2 mM DTT, and 2 mM EGTA and were concentrated to 4 mg/ml for crystallization. Crystallization trials were performed using the hanging-drop vapor-diffusion method at 20°C. The MICU1–MICU2 crystals were grown in 4 μl drops consisting of 2 μl protein and 2 μl reservoir solution containing 0.2 M ammonium chloride and 5% (w/v) polyethylene glycol (PEG) 3350. For the T4L-MICU1–MICU2 protein, the crystallization condition was 2% tacsimate pH 5.0, 0.1 M sodium citrate pH 5.0, and 12% (w/v) PEG 3350. The drops were sealed in a 24-well plate and equilibrated against 0.5 ml reservoir solution. Crystals of both proteins grew to diffraction size in 1 week and were cryo-protected (by supplementing 30% glycerol in the case of MICU1–MICU2 and 20% glycerol in the case of T4L-MICU1–MICU2 in their corresponding reservoir solutions) before flash freezing in liquid nitrogen. The diffraction data were collected at a wavelength of 0.979 Å under 100 K in the BL19U beamline at the Shanghai Synchrotron Radiation Facility (SSRF), and each dataset consisted of 720 frames with a 0.5° oscillation per frame (Wang *et al*, 2018).

Structure determination and refinement*

The X-ray diffraction datasets of both structures were indexed, integrated, and scaled using the program HKL2000 (Minor *et al*, 2006). Data quality was subsequently assessed using phenix.xtriage (Adams *et al*, 2010). For the MICU1–MICU2 structure, the model

was determined by molecular replacement (MR) using phenix.-phaser (Adams *et al*, 2010) and MICU1 (PDB code: 4NSC) and MICU2 (PDB code: 6IIH) to simultaneously search. Although one of the heterodimer molecules in the asymmetric unit was successfully located, only MICU2 was found in the second heterodimer. Further MR efforts located the N-lobe of MICU1. At this time, we resorted to the superimposition of the first MICU1–MICU2 molecule with the partial structure of the second molecule, which finally enabled the localization of the missing C-lobe. For the apo T4L-MICU1–MICU2 complex structure, the model was determined by MR simultaneously using the Ca^{2+}-free MICU1–MICU2 molecule and T4L probes. Relevant amino acid side chains were rebuilt based on the $2F_{obs}$-F_{calc} and F_{obs}-F_{calc} maps using Coot (Emsley *et al*, 2010). The structures were refined by phenix.refine (Adams *et al*, 2010). Detailed data collection and structure refinement statistics are summarized in Table 1.

Table 1. Data collection and refinement statistics for MICU1-MICU2 heterodimers.

Crystal name	MICU1–MICU2 (6LB7)	T4L-MICU1–MICU2 (6LB8)
Data collection		
Space group	$P2_12_12_1$	$P2_12_12_1$
Unit cell		
a, b, c (Å)	$a = 85.481$	$a = 79.339$
	$b = 107.721$	$b = 133.296$
	$c = 170.381$	$c = 178.023$
α, β, γ (°)	$\alpha = 90$	$\alpha = 90$
	$\beta = 90$	$\beta = 90$
	$\gamma = 90$	$\gamma = 90$
Wavelength (Å)	0.978	0.978
R_{merge} (%)[a]	0.1246 (1.192)	0.1947 (0.505)
I/σ/[a]	10.87 (1.35)	15.12 (4.43)
CC1/2	0.984 (0.775)	0.958 (0.937)
Completeness (%)[a]	0.98 (1.00)	0.99 (1.00)
Redundancy[a]	13.0 (12.3)	13.0 (12.9)
Refinement		
Resolution range (Å)[a]	47.3–2.101 (2.176–2.101)	49.06–3.283 (3.401–3.283)
Unique reflections[a]	92,168 (8,058)	29,560 (2,680)
R_{work}/R_{free} (%)[a]	(0.1939/0.2267) (0.2425/0.2451)	0.1835/0.2494 (0.2185/0.3460)
No. atoms		
Protein	9,893	12,694
Ligand/ion	2	0
B-factors		
Protein	35.3	39.88
Ligand or (solvent)	28.50	
R.m.s deviations (Å)		
Bond lengths (Å)	0.021	0.014
Bond angles (°)	1.29	1.29

[a]High-resolution shell is shown in parentheses.

*Note that the MICU1–MICU2 complex structures published here were deposited by the authors on PDB on November 13, 2019 [Accession numbers 6LB7 and 6LB8]. The related structure published in IUCr J. (Park *et al*, 2020) was deposited on PBD on November 24, 2019 [Accession number 6LE5].

Modeling of the fully Ca²⁺-bound structure

The fully Ca^{2+}-bound structural modeling of the MICU1–MICU2 complex was achieved using our partial Ca^{2+}-bound heterodimer structure (PDB code: 6LB7) and relevant Ca^{2+}-bound monomer structures. The partial Ca^{2+}-bound MICU1 was superimposed with the Ca^{2+}-bound MICU1 monomer (PDB code: 4NSD) by fixing the C-lobe (Ca^{2+}-bound lobe) of the partial Ca^{2+}-bound MICU1. The partial Ca^{2+}-bound MICU2 was superimposed with the fully Ca^{2+}-bound MICU2 monomer (PDB code: 6IIH, chain B) by fixing the N-lobe (Ca^{2+}-bound lobe) of the partial Ca^{2+}-bound MICU2. The fully Ca^{2+}-bound heterodimer was built by replacing the partial Ca^{2+}-bound MICU1 and MICU2 monomers with the fully Ca^{2+}-bound MICU1 and MICU2 monomers, respectively. The minimization of fully Ca^{2+}-bound model was achieved using Amber. The fully Ca^{2+}-bound system was solvated in the TIP3P water shell and neutralized with Na^+. The energy minimization was performed in two stages. In the first stage, only water molecules were minimized with the protein and Ca^{2+} fixed using $50 \text{ kcal}/(\text{mol·Å}^2)$ restraints. In the second stage, the entire system was minimized with maximum minimization cycle set to 200,000 steps. The first 1,000 steps were performed using steepest descent algorithm, followed by the conjugate gradient algorithm to reach minimal energy. The energy minimization process converged after 31,173 steps.

GST pull-down assays

The wild type and mutants of GST-MICU1 and GST-MICU2 were cloned into the pEGX-6p-1 vector between the BamHI and XhoI sites with an N-terminus GST-tag. Taking GST-MICU1 wild type pulled down MICU2 mutants (referred to as MICU2^mut) as an example, GST-MICU1 and MICU2^mut pellet were co-lysed in buffer I (see the protein purification section) with 2 mM EGTA or $CaCl_2$. Cell lysis and centrifugation procedures were the same as described above in the protein purification section. The supernatant was incubated with GST magnetic beads for 2 h at 4°C, and the beads were washed with buffer V (20 mM HEPES pH 8.0, 300 mM NaCl, and 2 mM EGTA or $CaCl_2$) three times. The GST beads were resuspended in loading buffer, and SDS–PAGE was performed for analysis.

Isothermal titration calorimetry

The ITC assay was performed at 25°C using a VP-ITC instrument (GE MicroCal). The EMRE peptide was dissolved in buffer containing 20 mM HEPES pH 7.5, 300 mM NaCl, and 2 mM DTT at a final concentration of 1 mM. The MICU1–MICU2 complex was purified using the same buffer as the EMRE peptide and concentrated to 50 μM. EMRE peptide aliquots (2 μl each) were injected into the sample cell (300 μl) containing the MICU1–MICU2 complex for 16 times, with time intervals of 300 s. The heat absorbed/released integration analysis was performed using the MicroCal Origin software package.

Microscale thermophoresis

Microscale thermophoresis experiments were performed as previously reported (Wienken et al, 2010). MICU1 (56–444 aa) was fused with GFP at the C-terminus and purified in buffer containing 20 mM HEPES pH 7.5, 150 mM NaCl, 2 mM DTT, and 2 mM EGTA or $CaCl_2$. Before the experiments, the MICU1-GFP concentration was adjusted to achieve an optimal fluorescence range of 400–1,500 fluorescence units at the wavelength λ = 470 nm. The EMRE peptide was subjected to a serial twofold dilution starting from 1 mM for 12 times using the same buffer as MICU1-GFP. Each peptide gradient (10 μl) was mixed with MICU1-GFP (2× optimal concentration, 10 μl) at an equal volume. After waiting 5 min, the mixture was added to 12 capillaries. The thermophoresis experiments were measured using the LED excitation source at λ = 470 nm, and data analyses were performed using the software from the manufacturer.

Peptide competition assays in cells

To obtain the EMRE peptide that would target mitochondria, we introduced the following sequence to the N-terminus of the EMRE peptide: D-Arg–Dmt–Orn–Phe (D-Arg, D-arginine; Dmt, 2,6-dimethyl-L-tyrosine; Orn, ornithine, referred to as mt-EMRE) (Cerrato et al, 2015). We also conjugated the probe 5(6)-carboxytetramethylrhodamine (TAMRA) in the mt-EMRE peptide to detect the localization of EMRE peptide (referred to as TAMRA-mt-EMRE). HEK cells were grown on 24 mm coverslips. MEmerald-Mito-7 plasmid encoding for a mitochondria-targeting sequence as mitochondrial marker (mEmerald-Mito-7 was a gift from Michael Davidson; addgene plasmid # 54160) (Planchon et al, 2011) and mito-RFP-linker-GCaMP6 m (referred to as mt-riG6 m) (Li et al, 2020) were transfected using the lipofectamine 3000 transfection reagent (Invitrogen) for peptide localization and competition assays, respectively. Six hours after the transfection, cells were treated with 20 μM TAMRA-mt-EMRE (for mitochondrial localization assay) or 100 μM mt-EMRE and scramble (MARAMRRAFQK) peptides (for competition assay) and re-incubated for 24 h in complete medium (DMEM supplemented with 10% FBS and 1% penicillin and streptomycin) at 37°C, 5% CO_2. Before imaging, cells were washed three times with a solution containing 20 mM HEPES pH 8.0, 10 mM NaCl, 140 mM KCl, and 1 mM $MgCl_2$. The dishes containing 1 ml solution were imaged using a ZEISS observer Z1 microscope with a 40× oil immersion objective lens (NA 1.3) as previously described (Li et al, 2020). MEmerald-Mito-7 and TAMRA fluorescence experiments used the following excitation/emission filter settings: 457–484 nm_{Ex}/580–678 nm_{Em} for mEmerald-Mito-7; 539–557 nm_{Ex}/580–678 nm_{Em} for TAMRA. To obtain mt-riG6 m ratio signal, filters for GCaMP6 m (457–484 nm_{Ex}; 497–525 nm_{Em}) and RFP (539–557 nm_{Ex}; 580–678 nm_{Em}) were used. After establishing 40 s baseline in 1 mM Ca^{2+} bath solution, 100 μM carbachol was added and images were taken sequentially for 6 min. The corresponding fluorescence readings from regions of interest were exported from the Zen software and imported into Matlab 2014a (The MathWorks, Natick, MA, USA) to calculate the F_{GCaMP}/F_{RFP} ratio. Ratio data and statistics were then plotted with Prism7 software. At least three independent repeats were performed.

Measurement of cytoplasmic Ca²⁺ clearance

Measurement of cytoplasmic Ca^{2+} concentration was done by following the published protocol (Mallilankaraman et al, 2012b). U2OS or HeLa cells were grown on glass-bottom imaging dishes. After culturing for 12 h, cells were treated with 100 μM mt-EMRE peptides and re-incubated for 24 h. Cells were washed with PBS three times and loaded with 5 μM fluo-4 probe in PBS for 30 min. In order to facilitate entry of the fluo-4 probe into the cells and avoid aggregation, 0.005% pluronic F127 was added. The dishes were mounted in an objective table at 37°C and imaged every 2 s at 488 nm excitation using a 60× oil objective (Nikon, A1). After establishing 50 s baseline, 100 μM histamine was added and image was taken sequentially for 3 min. Images were analyzed by NIS-Elements analysis software.

Data availability

The structures produced in this study are available in the following database: protein atomic coordinates data: PDB 6LB7 and 6LB8 (https://www.rcsb.org/structure/6lb7 and https://www.rcsb.org/structure/6lb8).

Expanded View for this article is available online.

Author contributions

WW, QS, JZ, and ZJ came up with the concept and designed the methodology. QS and WW collected data and determined the structures. WW and RZ performed the ITC, MST, and GST pull-down interaction experiments. YW, WW, and ZQ preformed the cells experiments. All authors analyzed data. WW, JZ, and ZJ wrote the manuscript.

Conflict of interest

The authors declare that they have no conflict of interest.

References

Adams PD, Afonine PV, Bunkoczi G, Chen VB, Davis IW, Echols N, Headd JJ, Hung LW, Kapral GJ, Grosse-Kunstleve RW et al (2010) PHENIX: a comprehensive Python-based system for macromolecular structure solution. Acta Crystallogr D Biol Crystallogr 66: 213–221

Ahuja M, Muallem S (2014) The gatekeepers of mitochondrial calcium influx: MICU1 and MICU2. EMBO Rep 15: 205–206

Balaban RS (2009) The role of Ca(2+) signaling in the coordination of mitochondrial ATP production with cardiac work. Biochem Biophys Acta 1787: 1334–1341

Baradaran R, Wang C, Siliciano AF, Long SB (2018) Cryo-EM structures of fungal and metazoan mitochondrial calcium uniporters. Nature 559: 580–584

Baughman JM, Perocchi F, Girgis HS, Plovanich M, Belcher-Timme CA, Sancak Y, Bao XR, Strittmatter L, Goldberger O, Bogorad RL et al (2011) Integrative

genomics identifies MCU as an essential component of the mitochondrial calcium uniporter. *Nature* 476: 341−345

Cerrato CP, Pirisinu M, Vlachos EN, Langel U (2015) Novel cell-penetrating peptide targeting mitochondria. *FASEB J* 29: 4589−4599

Chaudhuri D, Sancak Y, Mootha VK, Clapham DE (2013) MCU encodes the pore conducting mitochondrial calcium currents. *Elife* 2: e00704

Csordas G, Golenar T, Seifert EL, Kamer KJ, Sancak Y, Perocchi F, Moffat C, Weaver D, de la Fuente Perez S, Bogorad R *et al* (2013) MICU1 controls both the threshold and cooperative activation of the mitochondrial Ca(2) (+) uniporter. *Cell Metab* 17: 976−987

De Stefani D, Raffaello A, Teardo E, Szabo I, Rizzuto R (2011) A forty-kilodalton protein of the inner membrane is the mitochondrial calcium uniporter. *Nature* 476: 336−340

Denton RM (2009) Regulation of mitochondrial dehydrogenases by calcium ions. *Biochem Biophys Acta* 1787: 1309−1316

Duchen MR, Verkhratsky A, Muallem S (2008) Mitochondria and calcium in health and disease. *Cell Calcium* 44: 1−5

Emsley P, Lohkamp B, Scott WG, Cowtan K (2010) Features and development of Coot. *Acta Crystallogr D Biol Crystallogr* 66: 486−501

Fan C, Fan M, Orlando BJ, Fastman NM, Zhang J, Xu Y, Chambers MG, Xu X, Perry K, Liao M *et al* (2018) X-ray and cryo-EM structures of the mitochondrial calcium uniporter. *Nature* 559: 575−579

Fan M, Zhang J, Tsai C-W, Orlando BJ, Rodriguez M, Xu Y, Liao M, Tsai M-F, Feng L (2020) Structure and mechanism of the mitochondrial Ca2+ uniporter holocomplex. *Nature* 582: 129−133

Gifford JL, Walsh MP, Vogel HJ (2007) Structures and metal-ion-binding properties of the Ca2+-binding helix-loop-helix EF-hand motifs. *Biochem J* 405: 199−221

Gottschalk B, Klec C, Leitinger G, Bernhart E, Rost R, Bischof H, Madreiter-Sokolowski CT, Radulovic S, Eroglu E, Sattler W *et al* (2019) MICU1 controls cristae junction and spatially anchors mitochondrial Ca(2+) uniporter complex. *Nat Commun* 10: 3732

Kamer KJ, Mootha VK (2014) MICU1 and MICU2 play nonredundant roles in the regulation of the mitochondrial calcium uniporter. *EMBO Rep* 15: 299−307

Kamer KJ, Mootha VK (2015) The molecular era of the mitochondrial calcium uniporter. *Nat Rev Mol Cell Biol* 16: 545−553

Kamer KJ, Grabarek Z, Mootha VK (2017) High-affinity cooperative Ca(2+) binding by MICU1-MICU2 serves as an on-off switch for the uniporter. *EMBO Rep* 18: 1397−1411

Kamer KJ, Sancak Y, Fomina Y, Meisel JD, Chaudhuri D, Grabarek Z, Mootha VK (2018) MICU1 imparts the mitochondrial uniporter with the ability to discriminate between Ca(2+) and Mn(2). *Proc Natl Acad Sci USA* 115: E7960−E7969

Kamer KJ, Jiang W, Kaushik VK, Mootha VK, Grabarek Z (2019) Crystal structure of MICU2 and comparison with MICU1 reveal insights into the uniporter gating mechanism. *Proc Natl Acad Sci USA* 116: 3546−3555

Kirichok Y, Krapivinsky G, Clapham DE (2004) The mitochondrial calcium uniporter is a highly selective ion channel. *Nature* 427: 360−364

Li D, Wu W, Pei H, Wei Q, Yang Q, Zheng J, Jia Z (2016) Expression and preliminary characterization of human MICU2. *Biol Open* 5: 962−969

Li J, Wang L, Chen Y, Yang Y, Liu J, Liu K, Lee YT, He N, Zhou Y, Wang Y (2020) Visible light excited ratiometric-GECIs for long-term in-cellulo monitoring of calcium signals. *Cell Calcium* 87: 102165

Mallilankaraman K, Cardenas C, Doonan PJ, Chandramoorthy HC, Irrinki KM, Golenar T, Csordas G, Madireddi P, Yang J, Muller M *et al* (2012a) MCUR1 is an essential component of mitochondrial Ca2+ uptake that regulates cellular metabolism. *Nat Cell Biol* 14: 1336−1343

Mallilankaraman K, Doonan P, Cardenas C, Chandramoorthy HC, Muller M, Miller R, Hoffman NE, Gandhirajan RK, Molgo J, Birnbaum MJ *et al* (2012b) MICU1 is an essential gatekeeper for MCU-mediated mitochondrial Ca(2+) uptake that regulates cell survival. *Cell* 151: 630−644

Matesanz-Isabel J, Arias-del-Val J, Alvarez-Illera P, Fonteriz RI, Montero M, Alvarez J (2016) Functional roles of MICU1 and MICU2 in mitochondrial Ca(2+) uptake. *Biochem Biophys Acta* 1858: 1110−1117

Minor W, Cymborowski M, Otwinowski Z, Chruszcz M (2006) HKL-3000: the integration of data reduction and structure solution−from diffraction images to an initial model in minutes. *Acta Crystallogr D Biol Crystallogr* 62: 859−866

Nguyen NX, Armache JP, Lee C, Yang Y, Zeng W, Mootha VK, Cheng Y, Bai XC, Jiang Y (2018) Cryo-EM structure of a fungal mitochondrial calcium uniporter. *Nature* 559: 570−574

Opalinska M, Janska H (2018) AAA proteases: guardians of mitochondrial function and homeostasis. *Cells* 7: 163

Orrenius S, Zhivotovsky B, Nicotera P (2003) Regulation of cell death: the calcium-apoptosis link. *Nat Rev Mol Cell Biol* 4: 552−565

Paillard M, Csordas G, Huang KT, Varnai P, Joseph SK, Hajnoczky G (2018) MICU1 Interacts with the D-Ring of the MCU pore to control its Ca(2+) flux and sensitivity to Ru360. *Mol Cell* 72: 778−785

Park J, Lee Y, Park T, Kang JY, Mun SA, Jin M, Yang J, Eom SH (2020) Structure of the MICU1−MICU2 heterodimer provides insights into the gatekeeping threshold shift. *IUCrJ* 7: 355−365

Patron M, Checchetto V, Raffaello A, Teardo E, Reane DV, Mantoan M, Granatiero V, Szabo I, De Stefani D, Rizzuto R (2014) MICU1 and MICU2 finely tune the mitochondrial Ca2+ uniporter by exerting opposite effects on MCU activity. *Mol Cell* 53: 726−737

Patron M, Granatiero V, Espino J, Rizzuto R, De Stefani D (2018) MICU3 is a tissue-specific enhancer of mitochondrial calcium uptake. *Cell Death Differ* 26: 179-195

Payne R, Li C, Foskett JK (2020) Variable assembly of EMRE and MCU creates functional channels with distinct gatekeeping profiles. *iScience* 23: 101037

Perocchi F, Gohil VM, Girgis HS, Bao XR, McCombs JE, Palmer AE, Mootha VK (2010) MICU1 encodes a mitochondrial EF hand protein required for Ca (2+) uptake. *Nature* 467: 291−296

Petrungaro C, Zimmermann KM, Kuttner V, Fischer M, Dengjel J, Bogeski I, Riemer J (2015) The Ca(2+)-dependent release of the Mia40-induced MICU1-MICU2 dimer from MCU regulates mitochondrial Ca(2+) uptake. *Cell Metab* 22: 721−733

Phillips CB, Tsai CW, Tsai MF (2019) The conserved aspartate ring of MCU mediates MICU1 binding and regulation in the mitochondrial calcium uniporter complex. *Elife* 8: e41112

Planchon TA, Gao L, Milkie DE, Davidson MW, Galbraith JA, Galbraith CG, Betzig E (2011) Rapid three-dimensional isotropic imaging of living cells using Bessel beam plane illumination. *Nat Methods* 8: 417−423

Plovanich M, Bogorad RL, Sancak Y, Kamer KJ, Strittmatter L, Li AA, Girgis HS, Kuchimanchi S, De Groot J, Speciner L *et al* (2013) MICU2, a paralog of MICU1, resides within the mitochondrial uniporter complex to regulate calcium handling. *PLoS ONE* 8: e55785

Raffaello A, De Stefani D, Sabbadin D, Teardo E, Merli G, Picard A, Checchetto V, Moro S, Szabo I, Rizzuto R (2013) The mitochondrial calcium uniporter is a multimer that can include a dominant-negative pore-forming subunit. *EMBO J* 32: 2362−2376

Sancak Y, Markhard AL, Kitami T, Kovacs-Bogdan E, Kamer KJ, Udeshi ND, Carr SA, Chaudhuri D, Clapham DE, Li AA *et al* (2013) EMRE is an essential component of the mitochondrial calcium uniporter complex. *Science* 342: 1379−1382

Tomar D, Dong Z, Shanmughapriya S, Koch DA, Thomas
    T, Hoffman NE, Timbalia SA, Goldman SJ, Breves SL, Corbally
    DP *et al* (2016) MCUR1 is a scaffold factor for the MCU complex
    function and promotes mitochondrial bioenergetics. *Cell Rep* 15:
    1673−1685

Tsai MF, Phillips CB, Ranaghan M, Tsai CW, Wu Y, Willliams C, Miller C
    (2016) Dual functions of a small regulatory subunit in the mitochondrial
    calcium uniporter complex. *Elife* 5: e15545

Wang L, Yang X, Li S, Wang Z, Liu Y, Feng J, Zhu Y, Shen Y (2014) Structural
    and mechanistic insights into MICU1 regulation of mitochondrial calcium
    uptake. *EMBO J* 33: 594−604

Wang Q-S, Zhang K-H, Cui Y, Wang Z-J, Pan Q-Y, Liu K, Sun B, Zhou H, Li M-
    J, Xu Q *et al* (2018) Upgrade of macromolecular crystallography beamline
    BL17U1 at SSRF 29: 68

Wang Y, Nguyen NX, She J, Zeng W, Yang Y, Bai X-c, Jiang Y (2019) Structural
    mechanism of EMRE-dependent gating of the human mitochondrial
    calcium uniporter. *Cell* 177: 1252‑1261

Wienken CJ, Baaske P, Rothbauer U, Braun D, Duhr S (2010) Protein-binding
    assays in biological liquids using microscale thermophoresis. *Nat Commun*
    1: 100

Wu W, Shen Q, Lei Z, Qiu Z, Li D, Pei H, Zheng J, Jia Z (2019) The crystal
    structure of MICU2 provides insight into Ca(2+) binding and MICU1-
    MICU2 heterodimer formation. *EMBO Rep* 20: e47488

Xing Y, Wang M, Wang J, Nie Z, Wu G, Yang X, Shen Y (2019) Dimerization of
    MICU proteins controls Ca(2+) influx through the mitochondrial Ca(2+)
    uniporter. *Cell Rep* 26: 1203−1212

Yoo J, Wu M, Yin Y, Herzik MA Jr, Lander GC, Lee SY (2018) Cryo-EM structure
    of a mitochondrial calcium uniporter. *Science* 361: 506−511